Rotational Alignment in MnO*($A^6\Sigma^+$) from the Reaction Mn + O_2

Matthew A. Spence and Martin R. Levy*

Department of Chemical and Life Sciences, University of Northumbria, Ellison Place, Newcastle upon Tyne NE1 8ST, U.K.

Received: February 19, 1997; In Final Form: May 23, 1997[⊗]

The collision energy dependence of chemiluminescence, and its polarization relative to the initial velocity vector **k**, has been determined for MnO*($A^6\Sigma^+$) product from the Mn + O_2 reaction in the range 0−1500 kJ mol^{-1}. Analysis of the excitation function by the multiple line-of-centers approach indicates that three parallel processes, attributed to a^4D_J, z^8P_J (perhaps), and a^6D_J atoms, contribute. All seem to involve a significant excess barrier and a forward transition state shift with increasing collision energy, suggesting that reaction proceeds via inner ionic−covalent curve crossings at short internuclear distances. The measured alignments are relatively modest, indicating a predominant contribution to MnO rotation from O−O recoil in a nonlinear Mn−O−O configuration.

Introduction

As itemized in a recent review,[1] the alignment of products from bimolecular reactive collisions has been the subject of a number of investigations, dating back to the early 1970s. Techniques currently available have allowed measurement of the Legendre moment $\langle P_2(\hat{\mathbf{j}}'\cdot\hat{\mathbf{k}})\rangle$ ($\mathbf{j}'$ = product rotational angular momentum, $\mathbf{k}$ = reagent relative velocity) as a function not only of collision energy but of reagent orientation,[2−3] product vibrational[4] or vibrational−rotational state,[5−8] and even product Λ-doublet component.[9] Such experiments give particularly detailed information on the anisotropy of the forces involved in the reactive process.

Despite these advances, however, the number of reactions for which even an average value of $\langle P_2(\hat{\mathbf{j}}'\cdot\hat{\mathbf{k}})\rangle$ has been determined as a function of collision energy is relatively small. The overwhelming majority of studies have concerned reactions of alkali, alkaline earth, and metastable rare gas atoms,[1] and even here the maximum collision energy achieved is generally less than 100 kJ mol^{-1}. With the exception of reactions of the H + HL mass combination (H = heavy, L = light), it has therefore not been possible to follow the evolution of the alignment to the high energy limit.

Over the past few years, we have been conducting a systematic investigation at this laboratory into chemiluminescent reactions of manganese atoms. Using a laser-ablated beam of Mn atoms in various long-lived states (Table 1[10]), we have determined excitation functions from 0 to >1000 kJ mol^{-1} for reactions with N_2O,[11] O_2, NO_2, CO_2, SO_2,[12] $SnCl_4$,[13] $SiCl_4$,[14] SF_6,[15] CF_4,[16] F_2,[17] and Cl_2.[18] For the halogen-containing species, up to five different product channels have been detected. Analysis of those results in terms of a multiple line-of-centers model (MLC)[19] indicates that, in many cases, the reaction transition state shifts forward into the entrance valley with increasing collision energy.

We now turn our attention to product alignment in these reactions. In beam-gas experiments such as ours, the chemiluminescence technique is particularly well suited to determining $\langle P_2(\hat{\mathbf{j}}'\cdot\hat{\mathbf{k}})\rangle$. Measurement of the ratio of chemiluminescence intensity perpendicular and parallel to the beam axis **z**, $\rho = I_\perp/I_{||}$, yields the polarization index R with respect to **z**:

TABLE 1: Lowest-Lying Mn States[10]

state	excitation/kJ mol^{-1}
a^6S	0
a^6D_J	207 ± 4[a]
z^8P_J	222 ± 2[a]
a^4D_J	281 ± 2[a]

[a] Spin−orbit splitting.

$$R = \frac{1-\rho}{1+2\rho} \tag{1}$$

For a parallel-type electronic transition, it has been shown[20,21] that

$$R = -{}^1/_2\langle P_2(\hat{\mathbf{j}}'\cdot\hat{\mathbf{z}})\rangle \tag{2}$$

where, in the high-$\mathbf{j}'$ limit,[22]

$$\langle P_2(\hat{\mathbf{j}}'\cdot\hat{\mathbf{z}})\rangle = \langle P_2(\hat{\mathbf{j}}'\cdot\hat{\mathbf{k}})\rangle\langle P_2(\hat{\mathbf{k}}\cdot\hat{\mathbf{z}})\rangle \tag{3}$$

The azimuthal symmetry of beam-gas configurations allows the factorization (eq 3) of the alignment into dynamical and kinematic terms. $\langle P_2(\hat{\mathbf{k}}\cdot\hat{\mathbf{z}})\rangle$, the so-called "kinematic blurring" caused by the spread of reagent gas velocities, has been calculated in effusive beam-gas[22] and supersonic beam-gas experiments.[21] In Appendix A, we show that, in our pulsed beam-gas experiments, its value is anticipated to be ∼1.0, except at very low collision energies. Measurements of $\langle P_2(\hat{\mathbf{j}}'\cdot\hat{\mathbf{z}})\rangle$ therefore become equivalent to determination of $\langle P_2(\hat{\mathbf{j}}'\cdot\hat{\mathbf{k}})\rangle$.

We report here on our investigations of the reaction Mn + O_2 → MnO*($A^6\Sigma^+$) + O, whose fully ground-state channel is ∼124 kJ mol^{-1} endoergic.[23,24] Production of MnO*($A^6\Sigma^+$) requires an additional 214.2 kJ mol^{-1}.[25] Although our previous work here[12] was undertaken before the development of the MLC model, this represented a useful starting point for polarization measurements. In the first place, the MnO($A^6\Sigma^+ \rightarrow X^6\Sigma^+$) band system is well characterized[25−28] and is a parallel system, so that $\langle P_2(\hat{\mathbf{j}}'\cdot\hat{\mathbf{z}})\rangle$ can be extracted straightforwardly by eq 2. Second, from the practical point of view, alignment measurements were anticipated to be relatively straightforward as the chemiluminescence signals observed previously were certainly more intense than those found more recently in the Mn−halide reactions.

* Author to whom correspondence should be addressed.
[⊗] Abstract published in *Advance ACS Abstracts,* September 15, 1997.

S1089-5639(97)00632-4 CCC: $14.00

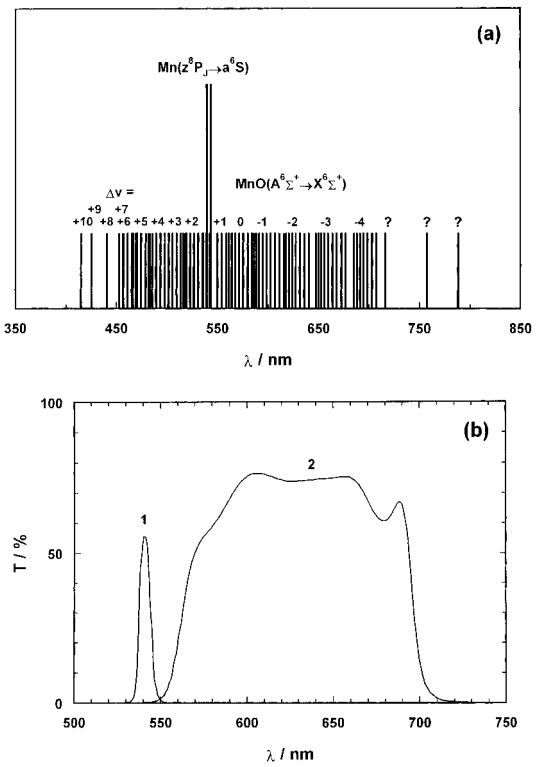

Figure 1. (a) Schematic of the known electronic spectroscopy of MnO.[25−28] The three bands marked ? at 716, 757, and 788 nm were observed in 1975 by Pinchemel and Schamps,[28] who reported that they appeared to form part of a separate system. Also shown is the position of the Mn $z^8P_J \rightarrow a^6S$ metastable emission observed from the atomic beam. (b) Filter transmission curves for (1) Mn atom beam emission at ∼540 nm and (2) MnO*($A^6\Sigma^+ - X^6\Sigma^+$) detection.

Since our previous work found evidence for the contribution of more than one reagent state to the observed chemiluminescence, the first necessity was to repeat and refine the excitation function measurements so that they could be deconvoluted by the MLC approach. These results are communicated below, along with the alignment measurements. However, in the course of the experiments, and in similar studies of the reactions Mn + NO_2, N_2O, CO_2, SO_2, and OCS,[29] we found that the emission extends much further into the IR than the known range of the MnO($A^6\Sigma^+ \rightarrow X^6\Sigma^+$) system and that both the excitation function and the collision energy dependence and sign of ρ in the IR differ from those found in the red region. Clearly we have two separate band systems.

As a result we have reviewed the existing literature on MnO electronic spectroscopy.[25−28] In a short paper from 1975 by Pinchemel and Schamps,[28] we find reference to three unidentified bands which they state do not form part of the $A^6\Sigma^+ \rightarrow X^6\Sigma^+$ system. Figure 1a illustrates the situation schematically. We had erroneously overlooked this reference previously[11,12] as it appeared that the IR signal was very small. In the present paper, therefore, we have restricted the wavelength range of observation to isolate the $A^6\Sigma^+ \rightarrow X^6\Sigma^+$ system. Our results for the IR system will be communicated separately.[29]

Experimental Section

For translational excitation function measurements, the apparatus and procedure are essentially the same as in our previous reports.[11,12] Briefly, a 10-Hz pulsed Mn atom beam is generated by focusing Q-switched 1064-μm radiation from a Nd:YAG laser onto a solid metal target *in vacuo*. At a distance x from the target, the beam interacts with a standing pressure of O_2 (typically ∼0.04 Pa), generating time-dependent chemiluminescence. An optical system, incorporating a cube beam splitter and suitable filter combinations, images chemiluminescence and long lived Mn*($z^8P_J \rightarrow a^6S$) metastable emission from the beam onto separate photomultipliers whose outputs are digitized (at 5-MHz sampling rate) and averaged on alternate shots. At any time t after the laser pulse, the *nominal* collision energy is given by $E_T^0 = {}^1/_2\mu(x/t)^2$, while the cross section $\sigma(E_T^0)$ is obtained from the ratio of chemiluminescence and beam signals, after taking account for metastable decay and relative detection efficiencies.

The filter transmission curves for the Mn* and MnO*($A^6\Sigma^+ \rightarrow X^6\Sigma^+$) emissions are shown in Figure 1b. The latter differs from that used previously because of the need to eliminate the IR band system. As noted before,[11] and as indicated in Figure 1, we are unable to collect emission from the whole of the MnO($A^6\Sigma^+ \rightarrow X^6\Sigma^+$) system since the Mn($z^8P_J \rightarrow a^6S$) metastable emission at ∼540 nm falls within it. However, as the filter combination transmits the $\Delta v = -4, -3, -2, -1$, and 0 progressions, we believe that the measurements are representative.

Before any alignment measurements could be undertaken, it was judged essential to eliminate external magnetic fields. Since the newly formed MnO* molecules have high spin, and hence high magnetic moments, they are expected to interact rapidly with even the relatively weak field of the Earth, $B \sim 5 \times 10^{-5}$ T, thereby scrambling any polarization of the emission. Therefore, three orthogonal pairs of Helmholtz coils were installed around the apparatus. The coils are constructed from series connection of either one or two turns of 20-core telecommunication cable mounted on octagonal aluminum frames of inner diameter 470 mm. With current adjustment, and by employing a Hall probe and Gauss meter (RFL Industries Inc., Model 750), the field at the reaction zone is adjusted to $\leq 5 \times 10^{-8}$ T in each of the X (vertical), Y (horizontal), and Z (horizontal—beam axis) directions. By retracting the Penning gauge a distance of 340 mm and adjusting its orientation, it was possible to minimize the Y and Z components of B before even using the coils. Operation of the coils was found to have no detectable effect on the photomulitplier sensitivity.

To obtain polarization ratios ρ, $I_\perp$ and $I_\parallel$ should in principle be measured by a single photomultiplier. However, this is not directly feasible in our experiment as the laser ablated Mn atom beam shows considerable shot-to-shot variation and an overall change in time-profile with increasing number of laser shots. Therefore, a pair of R928 photomultipliers, matched as closely as possible for gain and wavelength response, were employed, in the same configuration as for excitation function measurements. For each, an identical filter and polaroid combination was used, except (as necessary) for a 90° difference in orientation of the latter. The polaroids (Comar Instruments, HN32) were cut from adjacent pieces of sheet to ensure identical transmission properties.

Figure 2a shows the configuration. The vertically-mounted photomultiplier detects emission in the "straight-through" mode and the horizontally-mounted tube in the "reflected" mode. The polaroids are adjusted so that the vertical and horizontal photomultipliers observe emission polarized respectively perpendicular and parallel to **z**. However, two potential problems arise with this arrangement: first, the sensitivity of the photomultipliers can drift with time, and, second, while the beamsplitter (Melles Griot) is of the "nonpolarizing" variety, there may be subtle differences in the wavelength dependence of the *s*- and *p*-plane transmission in the two directions, which could invalidate any measurements of ρ.

These problems are resolved by referencing the "vertical"

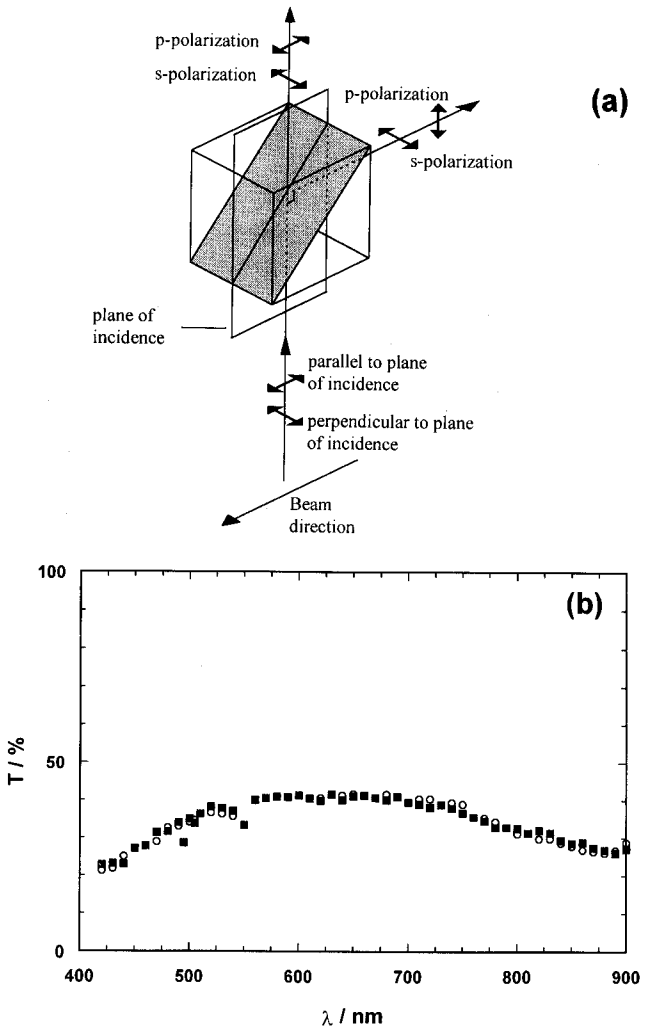

Figure 2. (a) Experimental configuration for polarization measurements. (b) Wavelength dependence of (■) p-plane (parallel-polarized) and (○) s-plane (perpendicular-polarized) transmission of the beam splitter in the straight-through (*i.e.* vertical) direction.

signal to the "horizontal": *i.e.*, we adjust photomultiplier gain so that the parallel-polarized signal intensities $I_{||}^{v}$, $I_{||}^{h}$ are comparable; then we make alternate measurements of ($I_{||}^{v}$, $I_{||}^{h}$) and ($I_{\perp}^{v}$, $I_{||}^{h}$). After averaging, these data are converted to ratios $I_{||}^{v}/I_{||}^{h}$ and $I_{\perp}^{v}/I_{||}^{h}$, from which ρ is obtained, as a function of time and hence E_T^0, by

$$\rho = (T_{||}^{v}/T_{\perp}^{v})\,(I_{\perp}^{v}/I_{||}^{h})/(I_{||}^{v}/I_{||}^{h}) \qquad (4)$$

where $T_{\perp}^{v}$, $T_{||}^{v}$ are the transmissions of the beam splitter cube for respectively perpendicular- and parallel-polarized light in the vertical (*i.e.*, "straight-through") direction. As shown in Figure 2b, we have measured $T_{\perp}^{v}$ and $T_{||}^{v}$, and the differences are insignificant in the present detection region. Eq 4 does, however, magnify the noise over that obtained for $\sigma(E_T^0)$, especially at long delay times, *i.e.*, at low values of E_T^0, where the signal is particularly small as a combined result of low beam intensity and low values of σ. High-quality polarization data therefore require many more laser shots than do comparable excitation function measurements.

Results and Analysis

The measured excitation function $\sigma(E_T^0)$ is displayed in panel (a) of Figure 3, while the corresponding yield function $Y(E_T^0) = E_T^0 \cdot \sigma(E_T^0)$ is shown in panel (b) and, expanded at low energies, in panel (c). Some 18 400 laser shots were employed here, compared with ~4000 previously.[12] The two $\sigma(E_T^0)$ data sets are superficially similar, but the peak is shifted to somewhat higher energies now that the IR band system has been excluded. The yield function plots indicate an initial threshold similar to that found previously but a delay in the onset of the more rapid rise.

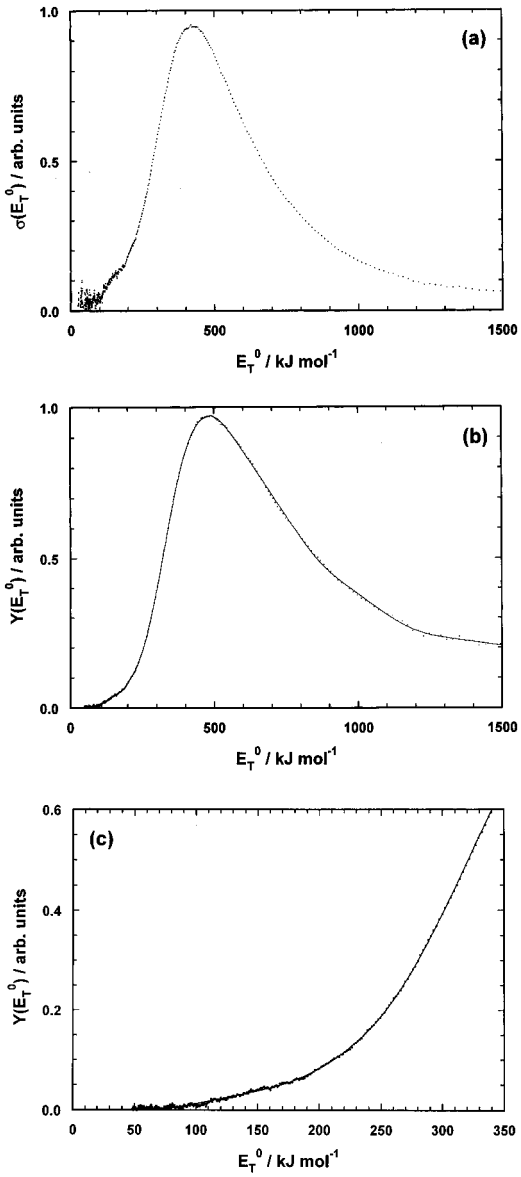

Figure 3. Collision energy dependence of (a) the chemiluminescence cross section $\sigma(E_T^0)$ and (b) the corresponding yield function $Y(E_T^0)$. In each case the data are arbitrarily normalized to near unity at the maximum. Panel (c) shows the low energy region of (b) to greater detail. The solid lines in (b) and (c) represent the least-squares best fit obtained on the basis of the MLC approach.

The results have been analyzed by means of the aforementioned MLC approach:[19]

$$\sigma(E_T) = \Sigma\sigma_k(1 - E_k/E_T) \qquad (5)$$

$$Y(E_T) = E_T \cdot \sigma(E_T) = \Sigma\sigma_k(E_T - E_k) \qquad (6)$$

where $k = 0, 1, 2, \ldots$, σ_k can be positive or negative ($k > 0$) and each term contributes only from its threshold E_k. In practice, the yield function form, which generates multilinear plots, is employed. Although we observe $\sigma(E_T^0)$ and calculate $Y(E_T^0) = E_T^0 \cdot \sigma(E_T^0)$, the latter differs from $Y(E_T)$ only by threshold curvature, which can be exactly calculated.[12,14]

TABLE 2: Parameters of the Excitation Function Analysis[a]

		k						
		0	1	2	3	4	5	6
I	σ_k	0.223 ± 0.006	0.57 ± 0.04	1.53 ± 0.04	−1.83 ± 0.05	−1.13 ± 0.05	0.325 ± 0.006	0.247 ± 0.006
	E_k	77 ± 1	192 ± 3	262 ± 2	398 ± 2	491 ± 3	866 ± 4	1186 ± 7
II	σ_k	0.250 ± 0.006	0.0090 ± 0.0003		−1.96 ± 0.06	−1.30 ± 0.04	0.324 ± 0.006	0.247 ± 0.006
	E_k	81 ± 1	190 ± 2	323 ± 5	384 ± 2	485 ± 2	866 ± 4	1190 ± 8

[a] I: straightforward MLC. II: modified MLC, with $n = 2$ process for $k = 1$; σ_k/arb. units, E_k/kJ mol^{-1}.

In the MLC interpretation, the overall shape of $\sigma(E_T)$ arises from competition between various production and depletion processes, each with its own impact parameter dependence. Thresholds with positive σ_k values before the onset of depletion are attributed to increases in reaction probability on the same potential surface or to the onset of new reaction paths, perhaps from different reagent states. Later positive σ_k values may, however, have a different origin, as explained below.

In previous studies,[13−19] two main types of depletion behavior—so-called "simple" and "complex"—have been observed. The former is characterized most straightforwardly by a two-term expansion of eq 5 or 6, in which $\sigma_1 \sim -\sigma_0$. We have explained this in terms of reaction with probability P_0 at internuclear distance R_0 and line-of-centers energy E_0, followed by depletion, with additional probability P_d, by trajectories penetrating with line-of-centers energy E_1 to internuclear distance R_d:

$$Y(E_T) = \pi P_0 R_0^2 (E_T - E_0) - \pi P_0 P_d R_d^2 (E_T - E_1) \quad (7)$$

from which $|\sigma_1/\sigma_0| = P_d R_d^2/R_0^2$, with $P_d \leq 1.0$.

Complex depletion typically involves three terms, with $\sigma_1 \sim -(\sigma_0 + \sigma_2)$, from which it appears that $R_d \gg R_0$. This rather strange behavior, however, is rationalized if a *forward transition state shift*, from R_0 to some new value R_s ($\sim R_d$), occurs at an energy $E_s \leq E_1$. Such a shift would not be apparent at first, since, in the absence of depletion or a reaction probability change, $\sigma(E_T)$ depends only on the maximum impact parameter for reaction. The shift only becomes visible when the functionality at R_s overtakes that at R_0, *i.e.*, at threshold E_2. If we write $\sigma_s = \pi P_0 R_s^2 = \sigma_0 + \sigma_2$, then, at $E_T > E_2$, eq 6 becomes

$$\begin{aligned} Y(E_T) &= \sigma_0(E_T - E_0) + \sigma_1(E_T - E_1) + \sigma_2(E_T - E_2) \\ &= \sigma_s(E_T - E_s) + \sigma_1(E_T - E_1) \\ &= \pi P_0 R_s^2 (E_T - E_s) - \pi P_0 P_d R_d^2 (E_T - E_1) \end{aligned} \quad (8)$$

from which

$$R_s/R_0 = (1 + \sigma_2/\sigma_0)^{1/2} \quad \text{and} \quad E_s\,(<E_1) = (\sigma_0 E_0 + \sigma_2 E_2)/\sigma_s \quad (9)$$

The MLC approach is clearly an approximation. As expressed above, it only allows for a line-of-centers type energy dependence, although other forms can be incorporated. We anticipated that such a modification might be necessary in the present case, since, in the previous work on this reaction, the yield function appeared to show "concave-up" curvature over a wide energy range, before finally becoming linear. On that occasion we had recourse to employ the microcanonical transition state theory (MTST) expression[30]

$$Y(E_T) = \sigma_0(E_T - E_0)^n \quad (10)$$

where n represents the number of vibrational−rotational modes active at the transition state. The data suggested one or two linear processes, with thresholds ∼60−70 and (perhaps) ∼118 kJ mol^{-1}, followed by an $n \sim 2$ process, with a threshold of ∼136−150 kJ mol^{-1}. These were attributed to reaction of a^4D_J, z^8P_J (perhaps), and a^6D_J metastable atoms, respectively.

In the present case, two linear rise regions, ∼75−180 and ∼280−350 kJ mol^{-1}, are clear, with a possible third in the range ∼190−230 kJ mol^{-1}. The curvature observed could be a consequence of either collision energy spread or an $n > 1$ process. In fact, we have been able to model the data using both the straightforward MLC approach and a modified form incorporating a single $n = 2$ process. The former assumes three linear rise processes, whereas the latter involves only one, followed by the $n = 2$ term (σ_1', E_1), becoming linear at energy E_2. This shift from $n = 2$ to $n = 1$ behavior, without a sudden break in slope, is modeled by including a second $n = 2$ term in the yield function expression when $E_T > E_2$:

$$\begin{aligned} Y(E_T) &= \sigma_0(E_T - E_0) + \sigma_1'(E_T - E_1)^2 - \sigma_1'(E_T - E_2)^2 + \ldots \\ &= \sigma_0(E_T - E_0) + 2\sigma_1'(E_2 - E_1)(E_T - {}^1/_2(E_1 + E_2)) + \ldots \end{aligned} \quad (11)$$

where $2\sigma_1'(E_2 - E_1)$ should be similar in magnitude to $(\sigma_1 + \sigma_2)$ for the straightforward MLC case.

For both forms, the effect of collision energy spread has been explicitly calculated, as indicated previously[12,14] (see Appendix B for the $n = 2$ case expression), and the best fit to $Y(E_T^0)$ has been obtained by nonlinear least squares regression.[31] The results, which are visually indistinguishable, are indicated by the solid lines in Figure 3, with the parameters of the analysis being displayed in Table 2. The normalization of the parameters applies to the excitation function in Figure 3a, although the back-calculated fit to $\sigma(E_T^0)$ is not displayed there as it would obscure the data points.

As can be seen, seven terms are needed in the straightforward MLC case: a lower number yields a poor fit to the low energy data, while an eight-term fit generates parameters which are not statistically valid. Outside the $n = 2$ region, the second fit has almost identical parameters to the first. In each case, $\chi^2 \sim 0.006$ and the correlation coefficient $r = 0.9999$, as might be expected from the close correspondence with the data. For the straightforward MLC fit, the off-diagonal elements of the correlation matrix are satisfactorily small, except for some correlation (within modest error limits) of σ_1 and σ_2 and also σ_3 and σ_4. For the modified fit, the only strong interparameter correlation is between σ_0 and E_0.

Clearly, the data could also be satisfactorily modeled by other modified MLC forms incorporating different values of n. However, it is notable that both the present forms indicate a production threshold at ∼190 kJ mol^{-1}, corresponding, as shown below, to a sharp change in the polarization ratio ρ, *i.e.*, the onset of a separate reaction channel. In fact, it is possible to decide between the two broad options. The large number of terms parallels the behavior in Mn + SF_6,[15] where consideration of the σ_k values allowed tentative deconvolution into three

TABLE 3: Tentative Excitation Function Deconvolution[a]

		k									
		0	1	2	3	4	5	6	7	R_s/R_0	E_s
a	σ_k	0.22				−0.28			0.06	1.13	
	E_k	77				491			≤2008		≤491
b	σ_k	σ_k	0.60			−0.85		0.25		1.19	
	E_k	E_k	192			491		1186			482
c	σ_k	σ_k		1.50	−1.83		0.33			1.10	
	E_k	E_k		262	398		866				368

[a] σ_k/arb. units; E_k, E_s/kJ mol^{-1}.

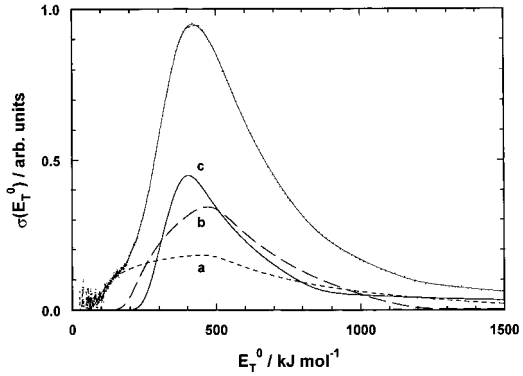

Figure 4. Tentative deconvolution of the data of Figure 3 into separate excitation functions **a** (---), **b** (− − −) and **c** (—) derived from the MLC analysis. The solid line through the data represents the sum of all three contributions.

reaction channels. Here, the unmodified MLC fit suggests an immediate, if partial, deconvolution since, within error limits, $\sigma_2 + \sigma_5 = -\sigma_3$, implying that these terms constitute a single channel. For the other fit, however, the limiting linear σ-coefficient $2\sigma_1'(E_2 - E_1) = 2.38$ is not offset by a negative σ_k value of equal or higher magnitude, hence it must be eliminated.

With this in mind, we present the tentative deconvolution in Table 3. The large negative slope of the yield plot at high energies implies that forward transition state shifts are involved. However, as in Mn + SF_6, it appears that there are two close E_k values, on separate channels, which we are unable to resolve (E_4). For the two higher-threshold channels **b** and **c**, application of eq 9 (with appropriate subscripts) leads to the values of R_s/R_0 and E_s given in the table, the latter being consistent with the corresponding E_d values. The continuing negative slope of the yield plot at $E_T^0 \sim 1500$ kJ mol^{-1} indicates that the secondary rise threshold E_7 for channel **a** is outside the range of our data. However, if we assume that $R_s/R_0 = R_d/R_0$, *i.e.*, $\sigma_7 = -(\sigma_0 + \sigma_4) = 0.06$, and $E_s \leq E_d$, then eq 9 leads to the upper limit given for E_7.

The excitation function curves corresponding to the separation in Table 3 are displayed in Figure 4. Although the overall deconvolution must be regarded as necessarily approximate, the individual contributions to the rise section (*i.e.*, $E_T^0 < 400$ kJ mol^{-1}) are quite clear.

The variation of polarization ratio ρ with collision energy is displayed in panel (a) of Figure 5. As expected for a $\Sigma-\Sigma$ band system, the data show a bias parallel to the Mn beam axis. At both ends of our energy range, however, there is a significant degree of noise. This arises primarily from the small signal to noise ratio, at both long and very short times, of $I_\perp^v$, $I_\parallel^v$, and $I_\parallel^h$, where the the beam intensity is very low and erratic, so that the uncertainty in the background level becomes significant. In particular, the ρ values >1.0 for $E_T^0 \leq 180$ kJ mol^{-1} are likely to be artifacts of the background level. The rapid, though modest, fall to ~0.92 at $E_T^0 \sim 200$ kJ mol^{-1} is, however, a genuine dynamical result.

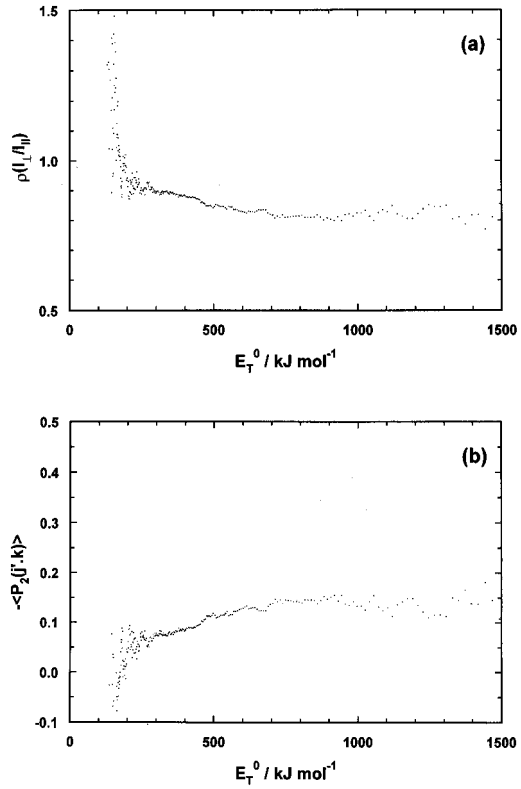

Figure 5. Translational energy dependence of (a) the polarization ratio of the emission ρ and (b) the corresponding MnO*($A^6\Sigma^+$) alignment.

Panel (b) displays the conversion of the data to $\langle P_2(\hat{\mathbf{j}}'\cdot\hat{\mathbf{k}})\rangle$ by means of eq 2. As shown in Appendix A, our measurement of $\langle P_2(\hat{\mathbf{j}}'\cdot\hat{\mathbf{z}})\rangle$ is essentially equivalent to $\langle P_2(\hat{\mathbf{j}}'\cdot\hat{\mathbf{k}})\rangle$ over the energy range employed. The results, however, represent the overall alignment $\langle P_2(\hat{\mathbf{j}}'\cdot\hat{\mathbf{k}})\rangle_{obs}$ from all contributing processes, *i.e.*,

$$\langle P_2\rangle_{obs} = \frac{\sum_i \sigma^i(E_T^0)\langle P_2\rangle^i}{\sigma(E_T^0)} \qquad (12)$$

where the superscripts *i* refer to the individual channels **a**, **b**, and **c**.

Below ~190 kJ mol^{-1}, only process **a** contributes. There does appear to be a small negative alignment, but, as discussed above, it is likely to be an artifact of the small signal and background uncertainty. In any case, $\langle P_2(\hat{\mathbf{j}}'\cdot\hat{\mathbf{k}})\rangle$ must be small. On the other hand, there is a sudden rise to ~0.07 at around 190 kJ mol^{-1}, the onset of channel **b**. Given the small contribution of channel **b** to $\sigma(E_T^0)$ at these energies, eq 12 suggests that it is, at least initially, much more highly aligned than **a**. However, the subsequent relative insensitivity of $\langle P_2(\hat{\mathbf{j}}'\cdot\hat{\mathbf{k}})\rangle_{obs}$ to collision energy, up to ~250 kJ mol^{-1}, implies that the alignment of channel **b** is in fact falling as E_T^0 rises.

Beyond this point, which corresponds to the threshold for channel **c**, $\langle P_2(\hat{\mathbf{j}}'\cdot\hat{\mathbf{k}})\rangle_{obs}$ rises slowly with increasing energy.

TABLE 4: Calculated Electron Jump Crossing Radii (Å)

$Mn^+ \rightarrow Mn$	a^7S	a^5S	a^5D_J	a^7P_J
a^6S	2.06	1.76	1.64	1.22
a^6D_J	2.97	2.39	2.17	1.50
z^8P_J	3.07	2.45	2.22	1.52
a^4D_J	3.53	2.73	2.45	1.63

While the tentative nature of the deconvolution means that definitive conclusions cannot be drawn about the behavior in each channel, it is significant that $-\langle P_2(\hat{\mathbf{j}}'\cdot\hat{\mathbf{k}})\rangle_{obs}$ never exceeds 0.15. Whatever the exact contributions from the different channels, therefore, it seems likely that all fall well short of the kinematic limit of 0.5 throughout the whole energy range.

Discussion

In ref 12, the minimum thresholds for production of MnO*($A^6\Sigma^+$) from Mn(a^4D_J, z^8P_J, a^6D_J, a^6S) + O_2 were calculated to be 54, 113, 128, and 335 (all ±8) kJ mol^{-1}, respectively. As before, therefore, the thresholds measured here completely exclude ground state atoms, and neither a^6D_J nor z^8P_J atoms can be responsible for the lowest energy process. Higher metastable states can be ignored since (i) their concentration in the beam will be very small and (ii) their participation is absent from all other reactions so far studied except Mn + D_2, CH_4, C_2H_2, and C_2H_4.[32,33] Unlike the present case, all of the latter are extremely endothermic covalent reactions. On the other hand, a^6D_J atoms have been clearly implicated in Mn + $SnCl_4$, $SiCl_4$, SF_6, and CF_4[13−16] with a probable contribution from z^8P_J atoms to the MnF*($A^7\Pi$) channel in the SF_6 case.

On that basis, therefore, thresholds **a** and **c** can be assigned to a^4D_J and a^6D_J atoms, respectively, with excess barriers of ∼23 and ∼134 kJ mol^{-1}. Since, as in Mn + SF_6, reaction of z^8P_J atoms would also be spin-allowed, this species could be the origin of threshold **b**. However, a^6D_J atoms cannot be excluded here since they were found, in Mn + $SiCl_4$, SF_6, to give rise to the same product state via more than one parallel channel. Whatever the reagent, the excess barrier for channel **b** will still be substantial: ∼79 kJ mol^{-1} for Mn*(z^8P_J) or ∼68 kJ mol^{-1} for Mn*(a^6D_J).

Since the MnO ground state is estimated to be Mn^+O^-,[34] we might expect interactions between ionic and covalent reagent potentials to play a role in the dynamics here. Indeed, as Menzinger has discussed for the alkaline earth−dihalogen reactions,[35] excited product states are likely to derive from "inner" crossings of covalent potentials with excited ionic surfaces. The lowest such surfaces in the present case are Mn^+*(a^5S,a^5D_J, z^7P_J) + O_2^-($^2\Pi$),[36] and the locations R_c of both "inner" and "outer" crossings, estimated by Magee's formula[37] on the basis of an O_2 electron affinity of 0.440 ± 0.008 eV,[38] are listed in Table 4 for different Mn electronic states. Such calculations are of course extremely crude, as both ionic species are assumed to be point charges, but they do at least indicate the relative accessibility of the different crossings.

As discussed below, the alignment measurements indicate a definite lack of preference for linear reaction geometry. In fact, for an initial covalent interaction, we might expect the preferred geometry to be a sideways approach of Mn to one O atom, since end-on or C_{2v} attack on O_2 will give zero net overlap with the partially filled π_g* orbital. Taking a 90° orientation, with R_c as the distance between the centers of Mn and the O−O bond (length 1.207 Å[23]), the a^5D_J radii in Table 4 suggest Mn−O distances of 1.53, 2.09, 2.14, and 2.38 Å for reaction of a^6S, a^6D_J, z^8P_J, and a^4D_J atoms, respectively. If a^5S surfaces are involved, these distances become 1.65, 2.31, 2.37, and 2.67 Å. All these values must, however, be regarded as upper limits

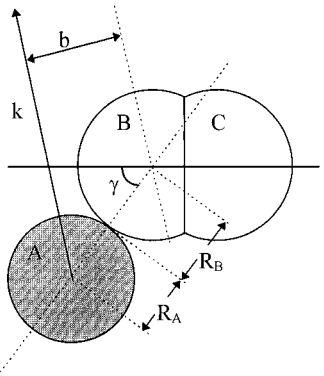

Figure 6. Angle-dependent hard sphere line-of-normals model of Gislason and Sizun.[45] The sizes of A and BC correspond (see text) to tabulated atomic and molecular dimensions for Mn + O_2.

owing to the extended charge distribution in O_2^-. In addition, as the Mn−O−O bond angle widens, the crossing radius will be reached only at progressively shorter Mn−O distances.

While the MnO bond length (1.648 and 1.714 Å for the $X^6\Sigma^+$ and $A^6\Sigma^+$ states respectively[25]) is within the range of most of these calculated values, the sum of the Mn atomic radius (1.18 Å[39]) and the O van der Waals radius (1.40 Å[39]) is somewhat higher. At the shortest distances calculated above, therefore, considerable repulsion would be anticipated from introduction of the second electron into the partially filled π_g* orbital. Even greater repulsion would be expected at wider angles than 90°. The excess thresholds observed here above the endothermicities and the absence of any ground state atom contributions are certainly consistent with such effects.

Avoided ionic−covalent curve crossings have been inferred previously[13−18] from the observation of forward transition state shifts, such as those seen here. In clearly covalent cases, *e.g.*, Mn + hydrocarbons,[33] such shifts are absent, but they have been found in most channels of all Mn−halogen/halide reactions investigated. To explain the effect, it was suggested: (i) that the crossings must lie in the exit valley, *i.e.*, at configurations in which the reagent bond length has stretched to something approaching that of the anion, and (ii) that, at elevated collision energies, there is insufficient time for the molecular bond to stretch, *i.e.*, the system cannot so easily "turn the corner" on the potential surface. As a result, there is a shift from "soft-sphere" to "hard-sphere" behavior, in which the vertical electron affinity, rather than the adiabatic value, becomes more important. A similar explanation would seem reasonable in the present case since a simple Morse function calculation based on the O_2 vibrational constants[23] indicates that an excitation of ∼46 kJ mol^{-1} would be required for stretching to the equilibrium bond distance in O_2^- (1.34 Å[40]).

Nonetheless, the line-of-centers threshold behavior observed here at first seems a little surprising, given that O_2 is not spherical. Various angle-dependent models[41−46] suggest an initial yield function dependence of the form of eq 10, with $n = 2$. Of these, the hard-sphere model of Gislason and Sizun,[45] illustrated in Figure 6 for the case A + BC, nonetheless provides a possible rationalization for the observed energy dependence. Their key points are (i) a barrier $E_0(\gamma)$ whose height depends on γ, the angle between the AB and BC bond directions, and (ii) an A−B line-of-normals, rather than A−BC line-of-centers, collision energy requirement,

$$E_T\{1 - b^2/(R_A + R_B)^2\} \geq E_0(\gamma) \qquad (13)$$

Here the impact parameter b refers to the distance between **k** and B rather than the center of BC, and **k** need not lie in the

plane of the atom centers. For B and C identical, eq 13 leads to

$$\sigma(E_T) = \int_{\gamma_{min}}^{\gamma_{max}} \sigma(\gamma,E_T) \sin\gamma \, d\gamma \quad (14)$$

where

$$\sigma(\gamma,E_T) = \pi(R_A + R_B)^2(1 - E_0(\gamma)/E_T) \quad (15)$$

and the limits of integration are defined by $E_T \geq E_0(\gamma)$. It follows that line-of-centers type behavior will be observed, within the resolution of our experiments, if $E_0(\gamma)$ is fairly insensitive to angle, or if the permitted angular range is fairly narrow. The former seems much less likely.

We now turn to the alignment results. As shown by Schechter *et al.*,[47] angular momentum conservation in an atom−diatom collision A + BC leads to

$$\mathbf{j}' = \sin^2\beta\mathbf{l} + \cos^2\beta\mathbf{j} + \cos^2\beta m_B(\mathbf{R} \wedge \dot{\mathbf{r}} + \mathbf{r} \wedge \dot{\mathbf{R}}) \quad (16)$$

where **l**, **j** are the initial orbital and rotational angular momenta, β is the skew angle given by

$$\cos^2\beta = \frac{m_A m_C}{(m_A + m_B)(m_B + m_C)} \quad (17)$$

and **r**, **R** are the vectors directed respectively from B to C and from the center of mass of BC to A. The third term in eq 16 is the impulse imparted during the switch over from reagents' to products' coordinates. $\dot{\mathbf{R}}$ and **k** are identical, while $\dot{\mathbf{r}}$ is parallel to **r** for BC vibration and perpendicular for rotation. Of course $\mathbf{l} = \mu_{A-BC}\mathbf{R} \wedge \mathbf{k}$ and $\mathbf{j} = \mu_{BC}\mathbf{r} \wedge \dot{\mathbf{r}}$.

Since we work with room temperature O_2, a Boltzmann distribution of reagent rotational states will be populated, peaking around $j = 8$.[23] Simple calculation then indicates that the magnitude of $\sin^2\beta\mathbf{l}$ will exceed that of the average $\cos^2\beta\mathbf{j}$ term if the product of the laboratory velocity v and the true impact parameter b_t > 160 ms^{-1}Å. In terms of the line-of-normals energy dependence discussed above, the reaction threshold corresponds to **k** lying along the A−B (Mn−O) line-of-centers, *i.e.*, the true impact parameter at threshold is 0.60 Å, half the O_2 bond length. For the ∼77 kJ mol^{-1} threshold, therefore, $vb_t \sim 1660$ ms^{-1}Å. On this basis, and in the absence of any contribution from the third term in eq 16, **j**′ will tend to be strongly aligned perpendicular to **k**. As collision energy increases, this effect will become even more marked since both v and the average value of b_t will be increasing together.

On the other hand, if the preferred geometry is nonlinear and recoil is significant, then the $\cos^2\beta m_B(\mathbf{R} \wedge \dot{\mathbf{r}} + \mathbf{r} \wedge \mathbf{R})$ term will tend to dominate eq 16. In fact, given the excess energy at all three production thresholds, O−O recoil ($\dot{\mathbf{r}}$) should be substantial, but in near-linear geometry the contribution of $\mathbf{R} \wedge \dot{\mathbf{r}}$ to **j**′ will be small. The $\mathbf{r} \wedge \dot{\mathbf{R}}$ term will increase as collision energy rises, but in a linear configuration this would simply give alignment perpendicular to **k**. In the nonlinear case, where MnO* rotation should be considerable, **j**′ should still be perpendicular to **k** at threshold, since **k**, **R**, **r**, and $\dot{\mathbf{r}}$ should be coplanar; however, at higher energies this requirement will not hold, so recoil will tend to make the alignment become increasingly isotropic.

Our results certainly suggest behavior of this sort. Where channel **a** alone contributes, the alignment is very small, implying that recoil dominates. Such threshold behavior as we are able to resolve, *i.e.*, channel **b**, implies a more substantial initial alignment, but then a fall with increasing energy, as expected. The rising trend of $-\langle P_2(\hat{\mathbf{j}}'\cdot\hat{\mathbf{k}})\rangle_{obs}$ at higher energies reflects the increasing magnitude of the $\sin^2\beta\mathbf{l}$ term in eq 16, but the failure to reach the maximum value of 0.5 indicates that O−O recoil in configurations noncoplanar with **k** still dominates all channels. Such behavior is not unsurprising since depletion will result in reaction becoming increasingly restricted to wide Mn−O impact parameters.

Conclusions

The collision energy dependence of chemiluminescence, and its polarization relative to the initial velocity vector **k**, has been measured for the MnO*($A^6\Sigma^+$) product from the Mn + O_2 reaction in the range $E_T^0 = 0-1500$ kJ mol^{-1}. The excitation function, $\sigma(E_T^0)$, has been satisfactorily modeled by both a seven-term multiple line-of-centers expression and a modified form incorporating an $n = 2$ microcanonical transition state theory process. Consideration of the best fit parameters has excluded the latter and allowed tentative deconvolution of the former into three parallel channels: **a**, **b**, and **c**. Process **a** appears to be due to a^4D_J atoms and **c** to a^6D_J, while either z^8P_J or a^6D_J atoms could be responsible for process **b**. All thresholds correspond to significant excess barriers to MnO* production.

The analysis indicates that each separate process involves a forward shift in transition state with increasing collision energy. From this it has been inferred that the mechanism involves an ionic−covalent curve crossing located toward the exit valley of the potential. It is suggested that as collision energy increases, the O_2 does not have time to stretch to the equilibrium distance in O_2^- and so a shift from "soft sphere" to "hard sphere" behavior occurs. Calculated crossing radii suggest that in the anticipated 90° preferred geometry, the interaction will be fairly repulsive, consistent with the observed excess barriers.

At low energies, where only the a^4D_J channel (**a**) contributes, the MnO* product is essentially unaligned. There is a sharp, if modest, increase in $-\langle P_2(\hat{\mathbf{j}}'\cdot\hat{\mathbf{k}})\rangle_{obs}$ at the threshold for process **b**, indicating that it is more highly aligned, although a fall off in that channel is implied thereafter. The threshold behavior for process **c** is not clear, but at higher energies the overall alignment increases only gradually with E_T^0, and does not exceed ∼0.15.

Such behavior indicates a predominant contribution to **j**′ from O−O recoil in a nonlinear Mn−O−O configuration. At threshold such dynamics will give strong alignment of **j**′ perpendicular to **k** since the latter vector will be coplanar with the atom centers. Above threshold, where **k** is no longer restricted to the plane, recoil will produce a more isotropic distribution. The increasing alignment at the highest energies reflects the growing influence of the orbital angular momentum **l**, although the fact that $-\langle P_2(\hat{\mathbf{j}}'\cdot\hat{\mathbf{k}})\rangle$ remains well below the theoretical maximum indicates that recoil still exerts a major influence on the dynamics in all channels.

Acknowledgment. We thank Professor J. M. Dyke for advice on Helmholtz coil construction and operation and Dr. I. D. Latimer for equipment loan. M.A.S. thanks the UK Engineering and Physical Sciences Research Council for a Research Studentship which enabled this work to be undertaken.

Appendix A: Kinematic Blurring

As noted above, $\langle P_2(\hat{\mathbf{k}}'\cdot\hat{\mathbf{z}})\rangle$, the so-called "kinematic blurring" caused by the spread of reagent gas velocities, has been calculated in effusive beam-gas[22] and supersonic beam-gas[21] experiments. There appears, however, to have been no attempt to address the configuration of our own experiments where

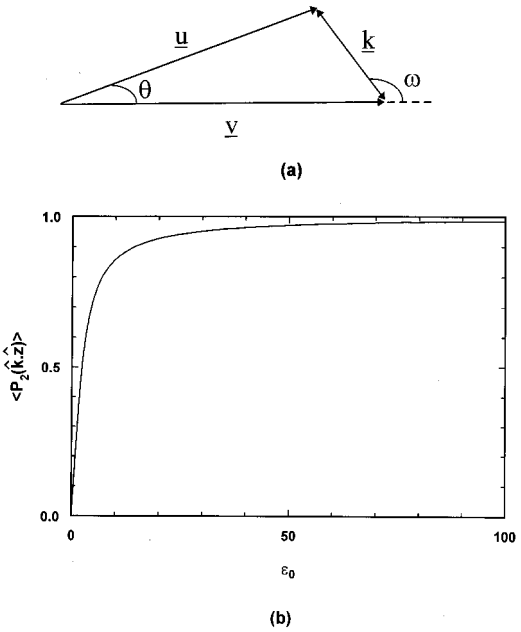

Figure 7. (a) Origin of kinematic blurring: **v** (= v$\hat{\mathbf{z}}$) and **u** are the Mn and O_2 laboratory velocities, while **k** is the resulting relative velocity. (b) Dependence of $\langle P_2(\hat{\mathbf{k}}\cdot\hat{\mathbf{z}})\rangle$ on scaled nominal collision energy $\epsilon_0 = E_T^0/\{m/(M + m)\}RT$ in this monoenergetic beam-thermal gas configuration.

essentially, at a given delay time, a monoenergetic beam interacts with a Maxwell−Boltzmann spread of reagent speeds in random directions.

Figure 7a illustrates the problem. For any given collision, the fixed beam velocity $\mathbf{v} = v\hat{\mathbf{z}}$, the gas velocity = **u**, and θ, ω are the angles between respectively **u** and **v** and **k** and **v**. Following Johnson *et al.*,[21] the kinematic blurring is given by

$$\langle P_2(\hat{\mathbf{k}}\cdot\hat{\mathbf{z}})\rangle = \int_{-1}^{1} P_2(\hat{\mathbf{k}}\cdot\hat{\mathbf{z}}) g(\hat{\mathbf{k}}\cdot\hat{\mathbf{z}})\, \mathrm{d}(\hat{\mathbf{k}}\cdot\hat{\mathbf{z}}) \qquad \text{(A1)}$$

where $g(\hat{\mathbf{k}}\cdot\hat{\mathbf{z}})$ is the distribution function over ω. As pointed out in ref 20, for velocity ratio $\eta = u/v$, elementary algebra yields

$$\hat{\mathbf{k}}\cdot\hat{\mathbf{z}} = \cos\omega = (1 - \eta\cos\theta)/(1 - 2\eta\cos\theta + \eta^2)^{1/2} \qquad \text{(A2)}$$

and $g(\hat{\mathbf{k}}\cdot\hat{\mathbf{z}})\,\mathrm{d}(\hat{\mathbf{k}}\cdot\hat{\mathbf{z}})$ can be represented by the probability function $P(\eta)P(\theta)\,\mathrm{d}\eta\,\mathrm{d}\theta$. We have

$$\mathrm{P}(\theta)\,\mathrm{d}\theta = {}^1/_2 \sin\theta\,\mathrm{d}\theta \qquad \text{(A3)}$$

and since

$$\mathrm{P}(u)\,\mathrm{d}u \propto \alpha^{3/2}u^2\exp(-\alpha u^2)\,\mathrm{d}u; \quad \alpha = M/2kT \qquad \text{(A4)}$$

where M, T are respectively the mass and temperature of the reagent gas molecules, then, for fixed v, and normalizing,

$$\mathrm{P}(\eta)\,\mathrm{d}\eta = (4/\pi^{1/2})\alpha^{3/2}v^3\eta^2\exp(-\alpha v^2\eta^2)\,\mathrm{d}\eta \qquad \text{(A5)}$$

The dimensionless quantity αv^2 is identical to the scaled nominal collision energy $\epsilon_0 = E_T^0/\{m/(M + m)\}RT$ (m = beam atomic mass) introduced by Chantry[48] and employed in our previous analysis of collision energy spread.[12]

Substituting for $P_2(\hat{\mathbf{k}}\cdot\hat{\mathbf{z}}) = {}^1/_2(3(\hat{\mathbf{k}}\cdot\hat{\mathbf{z}})^2 - 1)$ in eq A1, we obtain

$$\langle P_2(\hat{\mathbf{k}}\cdot\hat{\mathbf{z}})\rangle = (\epsilon_0{}^3/\pi)^{1/2}\int_0^{\pi}\sin\theta\int_0^{1/\cos\theta}\left\{\frac{3(1-\eta\cos\theta)^2}{1-2\eta\cos\theta+\eta^2} - 1\right\}\eta^2\exp(-\epsilon_0\eta^2)\,\mathrm{d}\eta\,\mathrm{d}\theta \qquad \text{(A6)}$$

where the limits of integration with respect to η are determined by the requirement $0 \le \eta \le 1/\cos\theta$. The result, obtained by numerical integration,[49] is plotted against ϵ_0 in Figure 7b. As can be seen, $\langle P_2(\hat{\mathbf{k}}\cdot\hat{\mathbf{z}})\rangle$ exceeds ~0.9 for $\epsilon_0 > 14$, reaching ~0.97 at $\epsilon_0 = 50$ and ~0.985 at $\epsilon_0 = 100$. For the Mn + O_2 system and our gas temperature of 300 K, these correspond to $E_T^0 \sim$ 22, 79, and 158 kJ mol^{-1}, respectively. Considering our observed initial thresholds of ~77 kJ mol^{-1}, it is clear that in the present system any kinematic blurring would have an insignificant effect on our measured alignments. We can therefore simply write $\langle P_2(\hat{\mathbf{j}}'\cdot\hat{\mathbf{k}})\rangle$ for $\langle P_2(\hat{\mathbf{k}}\cdot\hat{\mathbf{z}})\rangle$.

Appendix B: Transformed $n = 2$ Yield Function

The transformed versions, incorporating collision energy spread, of the general yield function expression eq 10 were given for $n = 1$, 2, and 3 in ref 12. As derived, these were presented in scaled energy units ϵ_0. Reference 14 gave the explicit unscaled form, incorporating the necessary conversion factors, in which the resulting MLC expression ($n = 1$) was used in analysis. Here we present the explicit form of the $n = 2$ version of eq 10. Writing $x \equiv E_T^0$, $f(x) \equiv Y(E_T^0)$, we get

$$f(x) = \sigma_0(c^{1/2}(0.5(E_0{}^{1/2} - x^{1/2})^3 + 2x^{1/2}(E_0{}^{1/2} - x^{1/2})^2 + (3x - E_0 + 0.75c)(E_0{}^{1/2} - x^{1/2}) + 2x^{1/2}(x - E_0 + c))\exp(-(E_0{}^{1/2} - x^{1/2})^2/c) + 0.5((x - E_0)^2 + (3x - E_0)c + 0.75c^2)\,\mathrm{erfc}((E_0{}^{1/2} - x^{1/2})/c^{1/2})) \qquad \text{(A7)}$$

where $c = \{m/(M+m)\}RT$. The change to linearity at some energy E_1 is then modeled by subtracting an identical expression with E_1 replacing E_0 (*cf.* eq 11).

References and Notes

(1) Orr-Ewing, A. J.; Zare, R. N. *Annu. Rev. Phys. Chem.* **1994**, *45*, 315.
(2) Jalink, H.; Parker, D. H.; Stolte, S. *J. Phys. Chem.* **1986**, *85*, 5372.
(3) Jalink, H.; Nicolaesen, G.; Stolte, S; Parker, D. H. *J. Chem. Soc. Faraday Trans. 2*, **1989**, *85*, 1115.
(4) Engelke, F.; Meiwes-Broer, K. H. *Chem. Phys. Lett.* **1984**, *108*, 132.
(5) Green, F.; Hancock, G.; Orr-Ewing, A. J. *Faraday Disc. Chem. Soc.* **1991**, *91*, 79.
(6) Costen, M. L.; Hancock, G.; Orr-Ewing, A. J.; Summerfield, D. *J. Chem. Phys.* **1994**, *100*, 2754.
(7) Brouard, M.; Duxon, S. P.; Enriquez, P. A.; Simons, J. P. *J. Chem. Phys.* **1991**, *95*, 8169.
(8) Brouard, M.; Duxon, S.; Enriquez, P. A.; Simons, J. P. *J. Chem. Soc. Faraday Trans.* **1993**, *89*, 1435.
(9) Kim, H. L.; Wickramaaratchi, M. A.; Zheng, X.; Hall, G. E. *J. Chem. Phys.* **1994**, *101*, 2033.
(10) Sugar, J.; Corliss, C. *J. Phys. Chem. Ref. Data* **1985**, *14*, Suppl. 2, 338ff.
(11) Levy, M. R. *J. Phys. Chem.* **1989**, *93*, 5195.
(12) Levy, M. R. *J. Phys. Chem.* **1991**, *95*, 8491.
(13) Herbertson, D. L.; Newnham, D. A.; Levy, M. R. *Can. J. Chem.* **1994**, *72*, 850.
(14) Newnham, D. A.; Levy, M. R. *J. Phys. Chem.* **1996**, *100*, 2799.
(15) Herbertson, D. L.; Levy, M. R. *J. Phys. Chem.* **1996**, *100*, 2809.
(16) Herbertson, D. L.; Levy, M. R. *J. Phys. Chem.* **1996**, *100*, 14584.
(17) Hughes, T. J.; Levy, M. R. *J. Phys. Chem.*, submitted.
(18) Hughes, T. J.; Levy, M. R., in preparation.
(19) Levy, M. R. *Res. Chem. Kinet.* **1993**, *1*, 163.
(20) Johnson, K.; Pease, R.; Simons, J. P. *Mol. Phys.* **1984**, *52*, 955.
(21) Zare, R. N. *Angular Momentum: Understanding Spatial Aspects in Chemistry and Physics*; Wiley: New York, 1988.

(22) Prisant, M. G.; Rettner, C. T.; Zare, R. N. *J. Chem. Phys.* **1981**, *75*, 2222.
(23) Huber, K.; Herzberg, G. *Constants of Diatomic Molecules*; Van Nostrand: New York, 1979.
(24) Smoes, S.; Drowart, J. *High Temp. Sci.* **1984**, *17*, 31.
(25) Gordon, R. M.; Merer, A. J. *Can. J. Phys.* **1980**, *58*, 642.
(26) Das Sarma, J. M. *Z. Phys.* **1959**, *145*, 98.
(27) Joshi, K. C. *Spectrochim. Acta* **1962**, *18*, 625.
(28) Pinchemel, B.; Schamps, J. *Can. J. Phys.* **1975**, *53*, 431.
(29) Spence, M. A.; Levy, M. R., to be published.
(30) González Ureña, A. *Mol. Phys.* **1984**, *52*, 1145.
(31) *Fig. P for Windows, Version 2.2*. Fig. P Software Corporation, Durham, NC.
(32) Levy, M. R. *Faraday Discuss. Chem. Soc.* **1991**, *91*, 168.
(33) Levy, M. R., to be published.
(34) Pinchemel, B.; Schamps, J. *Chem. Phys.* **1976**, *18*, 481.
(35) Menzinger, M. In *Gas Phase Chemiluminescence and Chemi-Ionization*; Fontijn, A., Ed.; Elsevier: New York, 1985; p 25.
(36) Younger, S. M.; Fuhr, J. R.; Martin, G. A.; Wiese, W. L. *J. Phys. Chem. Ref. Data* **1978**, *7*, 495.
(37) Magee, J. L. *J. Chem. Phys.* **1940**, *8*, 687.
(38) Lias, S. G.; Bartmess, J. E.; Liebman, J. F.; Holmes, J. L.; Levin, R. D.; Mallard, W. G. *J. Phys. Chem. Ref. Data* **1988**, *17, Suppl. 1*, 1
(39) James, A. M.; Lord, M. P. *Macmillan's Chemical and Physical Data*; Macmillan: London, 1982.
(40) Chase, M. W., Jr.; Davies, C. A.; Downey, J. R., Jr.; Frurip, D. J.; McDonald, R. A.; Syverud, A. N. *J. Phys. Chem. Ref. Data* **1985**, *14*, Suppl. 1.
(41) Smith, I. W. M. *J. Chem. Educ.* **1982**, *59*, 9.
(42) Levine, R. D.; Bernstein, R. B. *Chem. Phys. Lett.* **1984**, *105*, 467.
(43) Evans, G. T.; She, R. S. C.; Bernstein, R. B. *J. Chem. Phys.* **1985**, *82*, 2258.
(44) She, R. S. C.; Evans, G. T.; Bernstein, R. B. *J. Chem. Phys.* **1986**, *84*, 2204.
(45) Gislason, E. A.; Sizun, M. *J. Phys. Chem.* **1991**, *95*, 8462.
(46) Evans, G. T.; van Kleef, E.; Stolte, S. *J. Chem. Phys.* **1990**, *93*, 4874.
(47) Schechter, I.; Prisant, M. G.; Levine, R. D. *J. Phys. Chem.* **1987**, *91*, 5472.
(48) Chantry, P. J. *J. Chem. Phys.* **1971**, *55*, 2746.
(49) *Mathcad for Windows, Version 5.0*. Mathsoft Inc, Cambridge, MA.